A novel nonlinear constitutive model for rock: numerical assessment and benchmarking

R. Bustamante[1]*, S. Montero[1], A. Ortiz-Bernardin[1,2]

[1] Departamento de Ingeniería Mecánica, Universidad de Chile
Beauchef 851, Santiago Centro, Santiago, Chile

[2] Computational and Applied Mechanics Laboratory
Departamento de Ingeniería Mecánica, Universidad de Chile
Beauchef 851, Santiago Centro, Santiago, Chile

Abstract

In this article, we assess and benchmark a novel nonlinear constitutive relation for modeling the behavior of rock, in which the linearized strain tensor is a function of the Cauchy stress tensor. In stark contrast with the linearized theory of elasticity, the main feature of this novel nonlinear constitutive model is that a different behavior is obtained in compression than in tension, which is consisting with the experimental evidence. Four problems are solved using the finite element method: the compression of a cylinder, the biaxial compression of a slab with a circular hole and with an elliptic hole, and the shear of a slab with an elliptic hole. The results are compared with the predictions of the linearized theory of elasticity. In this comparison, it is found that the maximum stresses and their locations are significantly affected by the choice of the constitutive equation.

1 Introduction

Recently, new constitutive theories have been proposed for elastic bodies, wherein it is assumed that the stresses and the strains are found from implicit constitutive relations [22, 23, 27, 28]. These implicit relations are natural generalizations of the classical Cauchy and Green elastic bodies [31], wherein it is assumed that the stresses are given as functions of the strains. One subclass of constitutive equation that is found from the above implicit relations, corresponds to the case where the linearized (infinitesimal) strain tensor $\boldsymbol{\varepsilon}$ is a function (in general nonlinear) of the Cauchy stress $\boldsymbol{\sigma}$, i.e., $\boldsymbol{\varepsilon} = \mathfrak{h}(\boldsymbol{\sigma})$ (see [4, 24, 26]). As indicated, for example, in [7], such relatively new subclass of constitutive equation has many potential applications in the modelling of the behaviour of materials such as gum metal [10, 17], concrete [11] and rock [6]. In these examples, there are materials that can behave elastically and nonlinearly in the range of small strains and rotations.

For rock, it is well known from the experimental point of view that the behaviour of a sample under uniaxial compression differs from its behaviour under uniaxial tension, and if the Young's modulus is determined, it can be ten times higher in compression than in tension (see, for example, Table 1 in [12] and [1, 9, 20]). Additionally, for many distinct types of rock the behaviour of a sample under uniaxial load is nonlinear [14, 15, 3, 13, 19, 32, 29], which in some experiments is noticeable when the Young's modulus appears to be a function of the stress applied on such sample. Now, traditionally, in many practical applications involving the modelling of the mechanical behaviour of rock, researchers and engineers have used the linearized theory of elasticity to model such material, but different researchers have noticed that neglecting the above nonlinear behaviour

*Corresponding author. Fax:+56-2-6896057; e-mail: rogbusta@ing.uchile.cl

of rock can introduce large errors in the calculations (see, for example [18, 3, 12, 1], Section 6.6 of [9], and Sections 2.3.3 and 2.5.4 of [29], and references therein), particularly in the design of tunnel and underground opening, the drilling of well-bores, hydraulic fracturing, underground mining, and the perforation of deep wells. For this reason some researchers have proposed the use of some bilinear models for rock (see [12], and Chapters 6 and 7 in [9]), and also of some very simple nonlinear constitutive equations (see, for instance, [3] and Chapter 5 in [29]). The above models are not general and were proposed for very specific applications, such as the radial compression of a short cylindrical annulus (see Figure 8 in [3]). There is a need for a more general model to describe the nonlinear elastic behaviour of rock. Such a model is proposed in [6] assuming as a first approximation that rock is an elastic isotropic material.

In this work, the model proposed in [6] for rock is used in the solution of a series of two-dimensional boundary value problems using the finite element method. The problems are:

- The compression of a cylinder with different end conditions and assuming axial symmetry, which is studied in Section 3.
- In Section 4 results are presented for a slab with a circular hole under biaxial compression.
- A slab with an elliptic hole under biaxial compression, where the elliptical hole is used to approximately model a crack aligned with the horizontal axis is studied in Section 5.
- The same slab previously described subjected to a distant uniform shear stress field is analyzed in Section 6.

In Section 2, a short summary of the kinematics of deforming bodies and the equation of motion is presented. Also in that section, details on the constitutive equations, which were proposed in [6], are elaborated. Finally, in Section 7 we give some final remarks about the results presented in this article.

2 Basic equations

2.1 Kinematics and equation of motion

A particle in a body $\mathscr{B}$ is denoted by X and in the reference configuration $\kappa_R(\mathscr{B})$ it occupies the position $\mathbf{X} = \boldsymbol{\kappa}_R(X)$. In the current configuration $\kappa_t(\mathscr{B})$, the position of the point is denoted by $\mathbf{x}$, and it is assumed that there exists a one-to-one mapping $\boldsymbol{\chi}$ such that $\mathbf{x} = \boldsymbol{\chi}(\mathbf{X}, t)$. The deformation gradient, the left Cauchy-Green tensor, the displacement vector, and the linearized strain tensor are defined, respectively, as

$$\mathbf{F} = \frac{\partial \boldsymbol{\chi}}{\partial \mathbf{X}}, \quad \mathbf{B} = \mathbf{F}\mathbf{F}^{\mathrm{T}}, \quad \mathbf{u} = \mathbf{x} - \mathbf{X}, \quad \boldsymbol{\varepsilon} = \frac{1}{2}\left(\frac{\partial \mathbf{u}}{\partial \mathbf{x}} + \frac{\partial \mathbf{u}}{\partial \mathbf{x}}^{\mathrm{T}}\right). \tag{1}$$

The Cauchy stress tensor is denoted by $\boldsymbol{\sigma}$ and the local form of the balance of linear momentum is

$$\rho \ddot{\mathbf{x}} = \operatorname{div} \boldsymbol{\sigma} + \rho \mathbf{b}, \tag{2}$$

where ρ is the density of the body and $\mathbf{b}$ represents the specific body forces in the current configuration. More details on the above equations can be found in [30].

2.2 Constitutive relations

The constitutive equation to be used in this work was presented in [6], and is a subclass of a more general type of implicit relations of the form $\mathfrak{G}(\boldsymbol{\sigma}, \mathbf{B}) = \mathbf{0}$, which was proposed by Rajagopal and co-workers [22, 23, 27, 28, 25] for elastic bodies. Two special subclasses of the above implicit relation are the Classical Cauchy model, wherein the stress is assumed to be a function of the strains $\boldsymbol{\sigma} = \mathfrak{F}(\mathbf{B})$, and the new class $\mathbf{B} = \mathfrak{H}(\boldsymbol{\sigma})$. If the gradient of the displacement field is

assumed to be very small, from this last subclass of constitutive equation we obtain $\boldsymbol{\varepsilon} = \mathfrak{h}(\boldsymbol{\sigma})$, where it is observed that the linearized strain is a function of the stresses. Such constitutive equations could be used to study problems in fracture mechanics of brittle bodies, and in the modelling of concrete, gum metal and rock [11, 10, 17, 6]. As mentioned in the introduction, in the present communication, as a first approximation we consider rock to be an elastic and isotropic medium described by the constitutive equation $\boldsymbol{\varepsilon} = \mathfrak{h}(\boldsymbol{\sigma})$. We also assume the existence of a scalar function $\Pi = \Pi(\boldsymbol{\sigma})$ such that

$$\boldsymbol{\varepsilon} = \mathfrak{h}(\boldsymbol{\sigma}) = \frac{\partial \Pi}{\partial \boldsymbol{\sigma}}. \tag{3}$$

If we further assume that the function Π is isotropic, then $\Pi = \Pi(\sigma_1, \sigma_2, \sigma_3)$, where σ_p, $p = 1, 2, 3$ are the eigenvalues or principal stresses of $\boldsymbol{\sigma}$. The function Π must satisfy the symmetry conditions $\Pi(\sigma_1, \sigma_2, \sigma_3) = \Pi(\sigma_2, \sigma_1, \sigma_3) = \Pi(\sigma_1, \sigma_3, \sigma_2)$. To ensure a reasonable behaviour, additional restrictions on Π are presented in [5] and in Section 2.2.1 of [6]. From (3) we have

$$\boldsymbol{\varepsilon} = \sum_{p=1}^{3} \frac{\partial \Pi}{\partial \sigma_p} \mathbf{a}^{(p)} \otimes \mathbf{a}^{(p)}, \tag{4}$$

where $\mathbf{a}^{(p)}$ are the eigenvectors of $\boldsymbol{\sigma}$.

The results presented in Sections 3-6 will be compared against the results obtained for the classical linearized elastic model

$$\boldsymbol{\varepsilon} = \frac{(1+\nu)}{E}\boldsymbol{\sigma} - \frac{\nu}{E}(\mathrm{tr}\boldsymbol{\sigma})\mathbf{I}, \tag{5}$$

where E and ν are the Young's modulus and the Poisson ratio, respectively.

As in [6] the main experimental information to be used in the present study is Figure 4 of [15], where the axial deformation of a sample under compression assuming lateral constraint is documented[1]. One of the main considerations here is that the behaviour of rock is different under tension than compression The following expression for Π is used in this work (see Eq. (16) in [6]):

$$\begin{aligned}\Pi(\sigma_1, \sigma_2, \sigma_3) = \mathfrak{f}_1(\sigma_1) + \mathfrak{f}_1(\sigma_2) + \mathfrak{f}_1(\sigma_3) + \mathfrak{f}_2(\sigma_1)(\sigma_2 + \sigma_3) + \mathfrak{f}_2(\sigma_2)(\sigma_1 + \sigma_3) \\ + \mathfrak{f}_2(\sigma_3)(\sigma_1 + \sigma_2) + \mathfrak{f}_3\left(\frac{\sigma_1 + \sigma_2 + \sigma_3}{3}\right),\end{aligned} \tag{6}$$

where the functions $\mathfrak{f}_i$ were proposed in Eq. 69 of [6] and are given by

$$\mathfrak{f}_1(x) = \alpha_1 \left[d_1^{c_1 x} - c_1 \ln(d_1) x\right], \quad \mathfrak{f}_2(x) = \alpha_2 \left(d_2^{c_2 x} - 1\right), \quad \mathfrak{f}_3(x) = 3\alpha_3 \left[d_3^{c_3 x} - c_3 \ln(d_3) x\right], \tag{7}$$

where α_i, c_i and d_i, $i = 1, 2, 3$ are constants, whose values are presented in Table 1.

α_1 [MPa]	α_2	α_3 [MPa]	c_1 $\frac{1}{[\mathrm{MPa}]}$	c_2 $\frac{1}{[\mathrm{MPa}]}$	c_3 $\frac{1}{[\mathrm{MPa}]}$	d_1	d_2	d_3
0.011	-0.0004	0.001	-0.08	-0.05	-0.08	0.1	0.2	0.1

Table 1: Constants for the functions presented in (7).

Regarding the linearized model, the following values are used (see Eqs. 72-74 in [6]):

$$E \approx 2600\mathrm{MPa}, \quad \nu \approx 0.1038. \tag{8}$$

In Figure 1 results are shown for the axial component of the strain for the compression/tension of a cylinder using (6), (7) and the linearized the linearized theory of elasticity[2].

[1] From Table 1 of [12] we also have some information concerning the behaviour of different types of rock under tension, where the main result is that most types of rock are less stiff under tension than compression

[2] See Figure 3 in [6] and Figure 4 of [15].

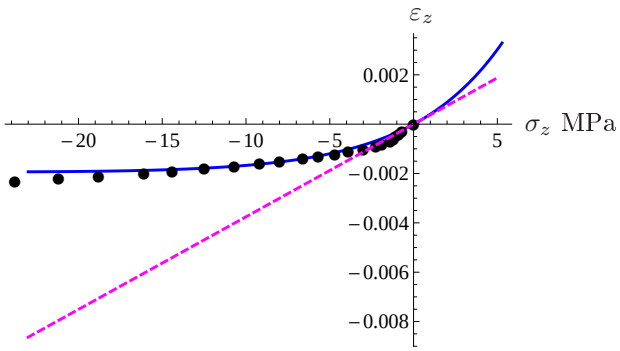

Figure 1: Uniform compression/tension of a cylinder. The blue line are results for the nonlinear model (6). The the black circles are experimental results taken from Figure 4 of [15]. The dashed magenta line indicates the results for the linearized model (6), (7).

2.3 Boundary value problem

For using (3) we need to find the displacement field $\mathbf{u}$ and the Cauchy stress tensor $\boldsymbol{\sigma}$ by solving

$$\rho\ddot{\mathbf{u}} = \operatorname{div}\boldsymbol{\sigma} + \rho\mathbf{b}, \quad \boldsymbol{\varepsilon} = \frac{1}{2}(\nabla\mathbf{u} + \nabla\mathbf{u}^{\mathrm{T}}) = \mathfrak{h}(\boldsymbol{\sigma}), \tag{9}$$

$$\boldsymbol{\sigma}\mathbf{n} = \hat{\mathbf{t}} \quad \mathbf{x} \in \partial\kappa_{\mathrm{r}}(\mathcal{B})_t, \quad \mathbf{u} = \hat{\mathbf{u}}, \quad \mathbf{x} \in \partial\kappa_{\mathrm{r}}(\mathcal{B})_u, \tag{10}$$

where, $\mathbf{n}$ is the unit normal vector to $\partial\kappa_{\mathrm{r}}(\mathcal{B})_t$, $\hat{\mathbf{t}}$ and $\hat{\mathbf{u}}$ are the external traction, and the specification of the displacement field, respectively, and $\partial\kappa_{\mathrm{r}}(\mathcal{B}) = \partial\kappa_{\mathrm{r}}(\mathcal{B})_t \cup \partial\kappa_{\mathrm{r}}(\mathcal{B})_u$ and $\partial\kappa_{\mathrm{r}}(\mathcal{B})_t \cap \partial\kappa_{\mathrm{r}}(\mathcal{B})_u = \emptyset$.

In the present work we consider only quasi-static deformations, therefore $\ddot{\mathbf{u}} = \mathbf{0}$. Additionally, to have (3) in a form suitable for a displacement-based finite element solver, Eq. (3) is inverted within the Newton-Raphson scheme (see [21] for more details on the numerical solution of (9)).

Finally, some plots are presented in a Supplementary Material, and the figures that appear in that file are cited as Figure iSM, which means Figure i in the Supplementary Material.

3 A cylinder under compression

In this section, a cylinder of circular cross section under compression is studied. We try to capture the actual interaction of the cylinder with the testing machine in a more precise manner. This is important because most of the experimental data for rock is obtained for compression tests on cylinders, where due to the interaction with the machine a non-homogeneous distribution of stresses and strains can appear inside the samples, which may be a source of errors when trying to find constitutive equations by fitting such data[3]. For example, in the plots presented in Figure 1 it was assumed that the cylinder deforms uniformly (see Section 3.1 in [6]).

In Figure 2(a), a depiction of one of the cases to be analyzed is shown, where after assuming axial symmetry the cylinder is simplified as a two-dimensional body. For that case (see the coordinate system in Figure 2(a)), we assume that the cylinder cannot move in the axial and the radial directions on the surface $z = 0$, $0 \leq r \leq r_{\mathrm{i}}$. Considering that in some testing machines it is easier to control the displacement being applied on the upper surface $z = L$, $0 \leq r \leq r_{\mathrm{i}}$, we assume that for that surface the axial displacement is known and given as u_{z_o} and that is uniform in the radial direction[4].

[3] See, for example, Figure 4.4 and Section 4.3.3 in [2], and pages 223, 225, 232, 259 and Figures 19 and 28(B) in [13].

[4] In reality from the point of view of causality an external traction is needed to cause u_{z_o}.

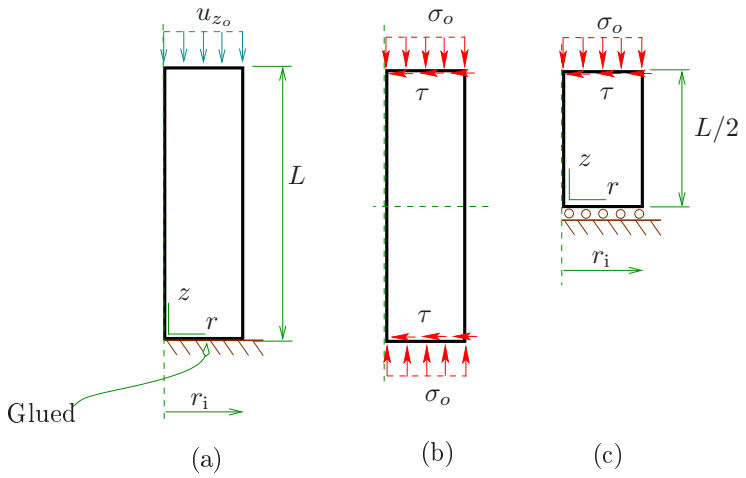

Figure 2: Axial-symmetric model of a cylinder under compression. (a) The cylinder is fixed on the surface $z = 0$, assuming that on the surface at $z = L$ the axial displacement u_{z_o} is prescribed. (b) The cylinder under compression assuming radial expansion and the appearance of shear stresses due to friction with the testing machine, and assuming that on the upper surface the axial stress σ_o is prescribed. (c) The problem presented in (b) using its symmetry in the axial direction.

In Figure 2(b), the second problem to be studied for the cylinder is schematically depicted, where axial symmetry is used and a uniform axial load σ_z is applied on the surface $z = L$, $0 < r < r_i$. On the surfaces $z = 0$, $z = L$, $0 < r < r_i$ the cylinder can expand radially but is subjected to the friction with the testing machine, which produces a shear stress τ. For symmetry reasons, the problem is set and studied as shown in Figure 2(c).

For the results presented in this section it is assumed that $L = 0.13\,\text{m}$, $r_{\rm i} = 0.025\,\text{m}$. Also in this section, the notation σ_r and σ_z is used to denote the radial and axial components of the stress that are in Pa, ε_{rr} and ε_{zz} are the radial and axial components of the strain tensor, and u_r, u_z are the radial and axial components of the displacement field. The following non-dimensional variables are used:

$$\bar{r} = \frac{r}{r_{\rm i}}, \quad \bar{z} = \frac{z}{L}, \quad \bar{u}_z = \frac{u_z}{L}. \tag{11}$$

3.1 Cylinder fixed on its bottom surface

Results are presented for the cylinder fixed on the surface $z = 0$ (see Figure 2(a)). On the surface $z = L$ it is assumed that the axial component of the displacement field u_z is given. In Figures 1-3SM results are presented for σ_z, σ_r and u_r for the case $u_z(r, L) = u_{z_o} = -3 \times 10^{-3}\,\text{m}$. The nonlinear constitutive equation (3) and the linearized equation (5) are used to compare the outcomes. From Figure 1SM it is observed that the axial component of the stress σ_z is almost constant for the whole cylinder but a zone near the bottom surface $z = L$. From Figure 2SM it is observed that the magnitude for the radial component of the stress is small for a large part of the cylinder (in comparison with the maximum values for that stress), with the exception of a zone near the bottom surface, which is something to be expected due to the fact that the cylinder is expanding radially but on that surface it cannot have radial and axial displacements. In both cases, there are differences in the distributions of stresses that result from the linearized (5) and nonlinear models (3). In particular, from Figure 2SM the stresses for the nonlinear case are higher (in magnitude) than the stresses obtained using the linear model. For the radial component of the displacement u_r, Figure 3SM shows, as expected, that the radial component is positive, its magnitude is larger near the outer surface, and is close to 0 near the axis $r = 0$. The distributions for the two cases are different. The magnitude is higher for the nonlinear model than for the

linear model, which is expected as in the nonlinear model the stiffness in tension is lower than in compression (see Figure 1 in [12] and Figure 4 and page 553 in [20]).

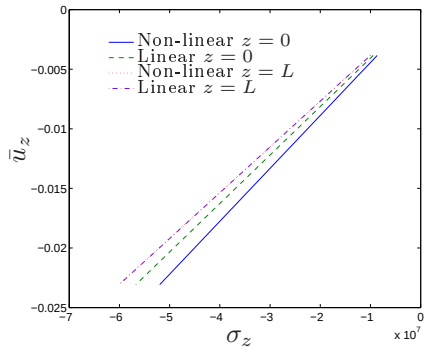

Figure 3: Axial dimensionless displacement $\bar{u}_z$ versus axial stress σ_z (in Pa) at two points, $(r, z) = (0, 0)$ and $(r, z) = (0, L)$, for a cylinder under compression (see Figure 2(a)) using the nonlinear model (3) and the linearized model (5).

In Figure 3, results are shown for the dimensionless axial component of the displacement field $\bar{u}_z$ as a function of the axial stress σ_z for two points inside the cylinder (see Figure 2(a)), namely $(r, z) = (0, 0)$ (the center of the cylinder on the lower part of it), and $(r, z) = (0, L)$ (the center of the cylinder on the upper surface).

From the results presented in Figure 3, there is a difference in the behaviour for the point located at the center of the lower surface (point $(r, z) = (0, 0)$) for the two models (3), (5). This difference in behaviour is due to the fact that from Figure 1 it is observed that the cylinder is stiffer in compression than in tension when using (3).

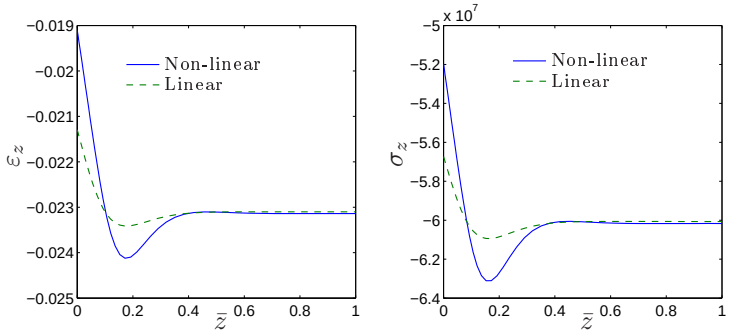

Figure 4: Comparison of the behaviour of ε_z and σ_z (in Pa) for the line $r = 0$, $0 \leq z \leq L$, when the non-linear model (Non-linear) (3) and the linearized model (Linear) (5) are used.

In Figure 4 results for ε_z and σ_z are shown for the line $r = 0$, $0 \leq z \leq L$, where a comparison between the nonlinear model (3) and the linearized model (5) is presented. In both cases it is observed that the behaviour of both variables is non-homogeneous near the bottom surface (near $z = 0$), where the cylinder is attached to the ground, and become constant far from that zone. The magnitude of ε_z and σ_z is higher for the nonlinear model (3).

Finally, several plots were made for the different components of $\boldsymbol{\varepsilon}$ and $\boldsymbol{\sigma}$ for the lines $z = L/2$, $0 \leq r \leq r_{\mathrm{i}}$ and $z = L$, $0 \leq r \leq r_{\mathrm{i}}$. It was found that most of the components of the strain and the stress tensors are almost constant (in r) for such lines, and there was not noticeable difference between the behaviour observed for the nonlinear model (3) and the linearized model (5). All such

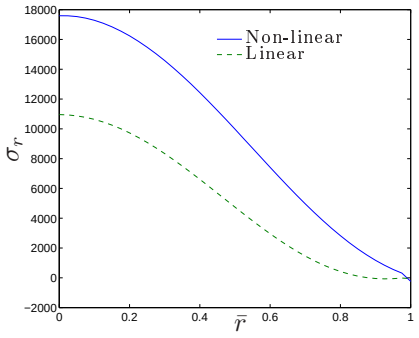

Figure 5: Comparison of the behaviour of σ_r (in Pa) for the line $z = L/2$, $0 \leq r \leq r_{\rm i}$, when the non-linear model (Non-linear) (3) and the linearized model (Linear) (5) are used.

plots are not shown here. In Figure 5, a plot for σ_r for the line $z = L/2$, $0 \leq r \leq r_{\rm i}$ is presented.

Comments

The compression/tension of a cylinder is one of the most important experiments used to determine the mechanical properties of solid media. An essential assumption to use the results of such experiment is that the stresses and strains are approximately uniform inside the cylinder, with the possible exception of small regions near the upper and lower surfaces of the cylinders. For rock, due to the characteristics of such brittle material, the experiment is usually performed in compression, and the cylinder is compressed between metal plates, which imposes restrictions on the radial displacement of the cylinder on such surfaces. As shown schematically in Figure 4.4(b) in [2], if the friction between rock and metal is very high, or if the cylinder is glued to such plates (complete radial constraint on such surfaces), a barreling is observed for the cylinders. Brady and Brown (see Section 4.3.3 in [2]) propose that $L/(2r_{\rm i}) \gtrapprox 2$ is necessary to have a good degree of uniformity inside the cylinder for the stresses and strains. For $L/r_{\rm i} = 13/5 > 2$, and from Figures 1-3SM, the distributions for σ_z, σ_r and u_r indeed appear to be approximately constant with the exception of a region about 20% of the length L near the lower surface. But such region of non-uniformity is larger when using the nonlinear model (3) (see in particular Figure 1SM).

In [13] there is also a detailed discussion on the effect of the end conditions, and we can compare, at least qualitatively, the results presented in Figure 4 (right) and Figure 5 with the distributions for the stresses in Figure 19 of [13] (recalling that $\sigma_x = \sigma_z$). The results are indeed similar, but for the nonlinear model (3) the magnitude of the stresses are larger, especially near $z = 0$ (the positions of the metal plates).

From Figure 4, we observe that ε_z and σ_z become almost constant in $\bar{z}$ if $\bar{z} \gtrapprox 0.4$. This is an important observation to adequately measure the strains in a place distant from that surface of the cylinder. Assuming a different behaviour in tension than in compression (see (3) and Figure 1) has a profound effect on the behaviour of σ_r as can be seen in Figure 5. The radial component of the stress increases in almost 60% of the value predicted by the linearized theory of elasticity (5).

3.2 Cylinder with radial expansion and friction

In this section results are presented for the problem depicted in Figure 2(c), where a cylinder under compression[5] is shown. On the upper and lower surfaces it is assumed that the cylinder can expand radially, but there is friction (see Figure 4.4(c) in [2]) that generates a shear stress on

[5] Figure 2(c) is a simplification of the original problem shown in Figure 2(b).

such surfaces. The shear stress is assumed to be proportional to the compressive load σ_o

$$\tau = \mu \sigma_o, \tag{12}$$

where $\mu = 0.35$ is the value used for the friction coefficient between rock and metal.

In Figure 4SM, results for σ_z (in Pa) when the external load on the upper surface of the cylinder is[6] $\sigma_o = -2 \times 10^7$ Pa are presented. On the left the results were obtained using the linearized constitutive equation (5), and on the right the results were obtained using the nonlinear model (3). From these results we observe that the behaviour of that component of the stress is rather non-homogeneous for a large part of that quarter of the cylinder (see Figure 2(c)). The distributions obtained with the linearized model differ from those of the nonlinear model. In both cases there are only compressive stresses. For the linearized model it is observed that the zone where σ_z is approximately constant is slightly larger than in the nonlinear model.

In Figure 5SM, results for σ_r (in Pa) are shown when the external load is $\sigma_o = -2 \times 10^7$ Pa. On the left the results were obtained using the linearized constitutive equation (5), and on the right the results were obtained using the nonlinear model (3). In contrast to the results presented in Figure 4SM , here for the zones where σ_r is non-homogeneous are smaller in both cases, especially for the linearized model (5). As it is expected in this problem, the radial stress should be close to 0 for most of the cylinder.

In Figures 6SM and 7SM results are shown for the axial and radial components of the displacement field $\mathbf{u}$. For the axial displacement it is observed that there are no differences between the results using the linear and nonlinear constitutive models. For the radial component of the displacement, the constitutive models (3) and (5) predict results that are different.

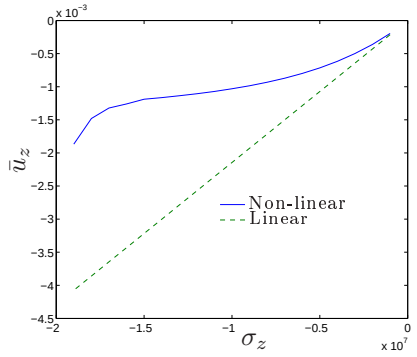

Figure 6: Axial dimensionless displacement $\bar{u}_z$ versus axial stress σ_z (in Pa) at point $(r, z) = (0, L/2)$ for a cylinder under compression (see Figure 2(c)) using the nonlinear model (3) and the linearized model (5).

Figure 6 presents the behaviour of the non-dimensional axial component of the displacement field $\bar{u}_z$ as a function of the axial (compressive) stress σ_z at the point $(r, z) = (0, L/2)$, where the results using the linearized model (5) and the new nonlinear constitutive equation (3) are compared. It is observed that the behaviour of the cylinder is stiffer when using the nonlinear model (3). This is because in the experimental results presented in [15], which were used to obtain (7), a sample of rock under compression tends to show some strain limiting behaviour[7].

In Figure 7, results are shown for the radial component of the strain ε_r and the stress σ_r for the line $z = 0$, $0 \leq r \leq r_i$. In both cases it is observed that when the linear constitutive model (5) is used, the results are almost constant, and in particular for the radial stress, they are approximately zero inside the cylinder. This is not the case when using the nonlinear model (3), where in particular the radial component of the stress can increase significantly inside the

[6] This was the maximum load that it was possible to apply without the radial strain ε_r becoming too large.
[7] See, for example, page 191 in [3], Figure 10 in [32] and page 208 in [29]

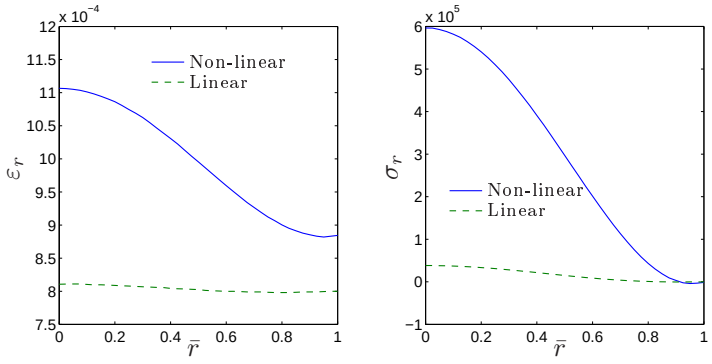

Figure 7: Comparison between the behaviour of ε_r and σ_r (in Pa) for the line $z = 0$, $0 \leq r \leq r_{\mathrm{i}}$ (see Figure 2(c)) when using the nonlinear model (Non-linear) (3) and the linearized model (Linear) (5).

cylinder. It is necessary to recall that for this cylinder under axial compression, in the radial direction there are positive radial strains, and the nonlinear constitutive model was formulated such that the behaviour of a cylinder under tension is less stiffer than in compression (see (3), (6) and (7)), which is the reason of the larger magnitude for ε_r in the nonlinear model.

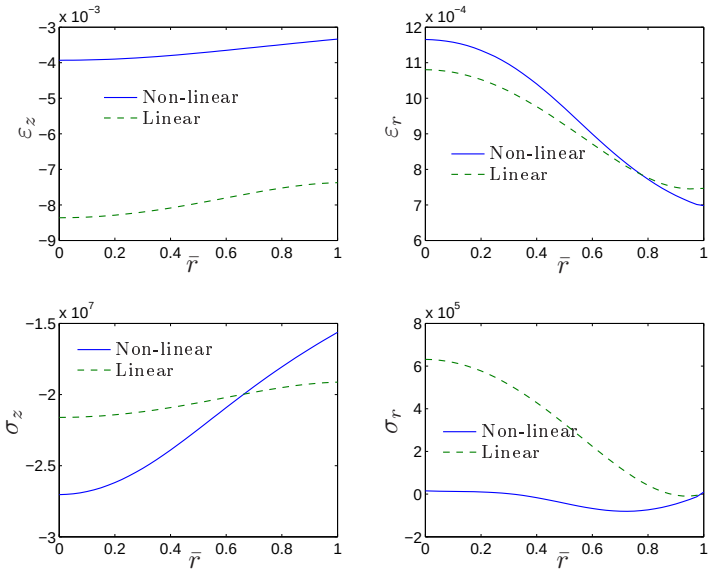

Figure 8: Comparison among the behaviour of ε_z, ε_r, σ_z (in Pa) and σ_r (in Pa) for the line $z = L/2$, $0 \leq r \leq r_{\mathrm{i}}$ (see Figure 2(c)) when using the nonlinear model (Non-linear) (3) and the linearized model (Linear) (5).

Finally, in Figure 8 results are presented for the line $z = L/2$, $0 \leq r \leq r_{\mathrm{i}}$ for the radial and axial components of the strain and stress.

Comments

The assumption that the upper and lower surfaces of the cylinder can expand radially, due to the presence of a shear stress, caused by the friction with the metal plates, implies also a markedly different behaviour between the results obtained using the nonlinear model (3) and the linearized constitutive equation (5) (see in particular Figures 6, 7 and 8). This is because rock is less stiffer in tension than in compression. From the results presented in Sections 3.1 and 3.2, it is observed that when more realistic boundary conditions are imposed for the cylinder under compression, the stresses and strains inside the body are non-homogeneous for both the nonlinear and linearized models.

4 Biaxial compression of a slab with a circular hole

An important problem in mining and geomechanics is the determination of stresses and strains for a rock mass with a circular hole under uniform vertical and horizontal loads. The rock mass

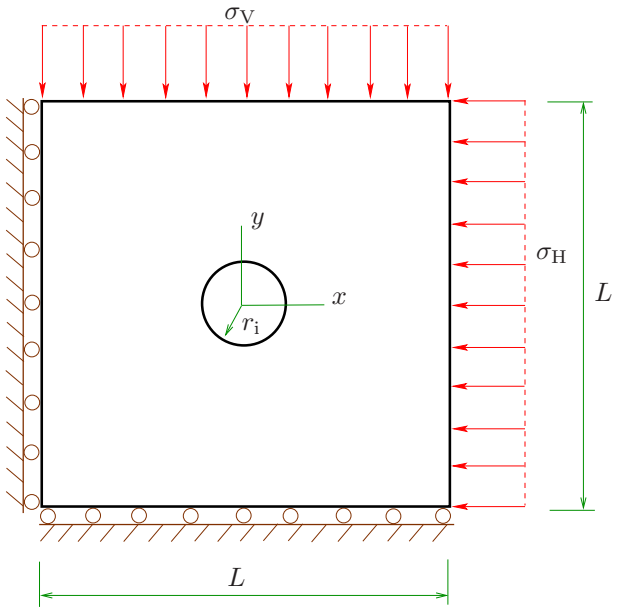

Figure 9: Slab with a central circular hole under biaxial compression.

is simplified as a slab of length and high L that is infinitely long in the direction z (see Figure 9), so that plane strain condition can be assumed. The hole of radius r_i can be considered as a simplified representation of a tunnel crossing the rock mass.

The stresses σ_V represent the effect of the weight above the slab, and the lateral uniform load σ_H is used to model the lateral interaction of the slab with the rest of the surroundings[8]. An important assumption is that the distribution of stresses is uniform far from the hole.

On the left side of the slab it is assumed there is no displacement in the direction x, whereas on the surface at the bottom of the slab it is assumed there is no vertical displacement in the direction y. The body load in the slab due to its own weight is not considered, i.e., $\mathbf{b} = \mathbf{0}$ (see $(9)_1$). Finally, the surface of the hole is free of external traction.

It is assumed that $L = 100\,\mathrm{m}$ and $r_i = 2.5\,\mathrm{m}$, then $L \gg r_i$. For σ_V and σ_H two cases are studied: when $\sigma_H = \sigma_V$, and $\sigma_H = 2\sigma_V$.

[8] Regarding $\sigma_{\mathbf{H}}$, it is possible to use a linear distribution in y to consider the effect of the weight of the surroundings rock masses in a more precise manner, but for simplicity this is not used in this work.

The following dimensionless variables are defined:

$$\bar{x} = \frac{x}{L}, \quad \bar{y} = \frac{y}{L}, \quad \bar{\sigma}_{11} = \frac{\sigma_{11}}{\sigma_{\mathrm{V}}}, \quad \bar{\sigma}_{22} = \frac{\sigma_{22}}{\sigma_{\mathrm{V}}}. \tag{13}$$

For the results presented in Figures 10-14 it is assumed that $\sigma_{\mathrm{V}} = \sigma_{\mathrm{H}}$.

Figures 9SM and 10SM present results for the slab under bi-axial compression with a hole assuming that[9] $\sigma_{\mathrm{V}} = -2 \times 10^7\,\mathrm{Pa}$. In Figure 9SM therein the behaviour in the slab differs between the two constitutive models. In particular, the absolute magnitude of σ_{22} is higher when using the nonlinear constitutive model (3).

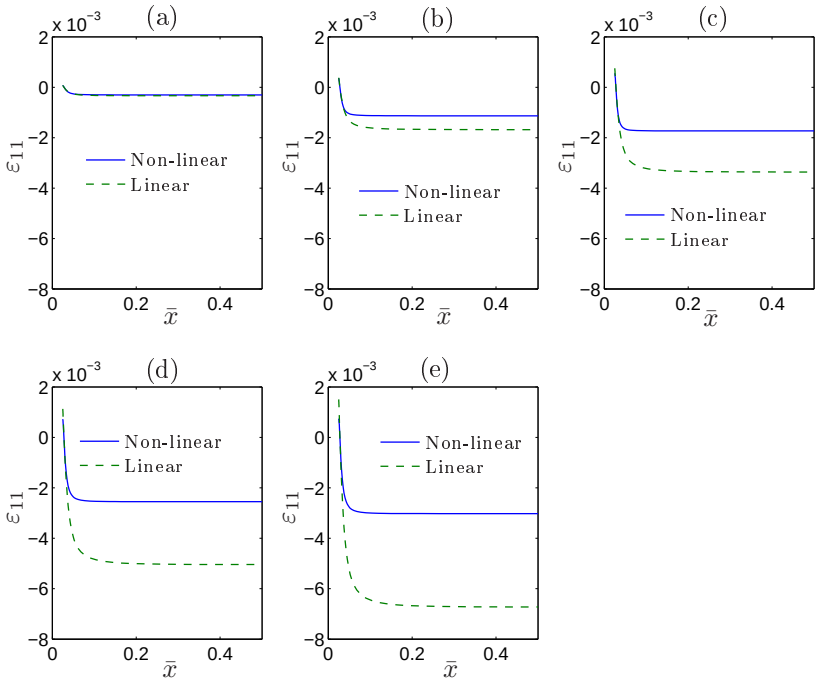

Figure 10: Behaviour of ε_{11} for $y = 0$, $0 \le x \le L/2$ when using the nonlinear model (Non-linear) and the linearized model (Linear). (a) $\sigma_{\mathrm{V}} = -10^6\,\mathrm{Pa}$, (b) $\sigma_{\mathrm{V}} = -5 \times 10^6\,\mathrm{Pa}$, (c) $\sigma_{\mathrm{V}} = -10^7\,\mathrm{Pa}$, (d) $\sigma_{\mathrm{V}} = -1.5 \times 10^7\,\mathrm{Pa}$, (e) $\sigma_{\mathrm{V}} = -2 \times 10^7\,\mathrm{Pa}$.

In Figure 10 the behaviour of $\varepsilon_{11}(x)$ is presented for the line $y = 0$, $0 \le x \le L/2$ (see Figure 9) for different external loads σ_{V}. The results obtained using the linear constitutive model (5) are compared with those of the nonlinear constitutive model (3). From these results, we observe that for higher values of σ_{V} there is a more notorious disagreement between the predictions of the two models.

In Figure 11, the behaviour of ε_{22} is presented using the linear and nonlinear models for the line $y = 0$, $0 \le x \le L/2$ and different external loads σ_{V}. In this case, the magnitude of ε_{22} is higher when the linear model (5) is used. It is observed that the maximum (in magnitude) for ε_{22} is not located at the boundary of the hole.

Results for $\bar{\sigma}_{11}$ and $\bar{\sigma}_{22}$ for the line $y = 0$, $0 \le x \le L/2$ are shown in Figures 12 and 13 for different external loads σ_{V}. Due to the traction-free condition near the boundary of the hole, $\bar{\sigma}_{11}$ is zero for $(x, y) = (r_{\mathrm{i}}, 0)$. Far from the hole, σ_{11} becomes uniform and is close to σ_{V} ($\bar{\sigma}_{11} \to 1$).

[9] This was the maximum external traction for which the strains are small within the small strain assumption of the model (3).

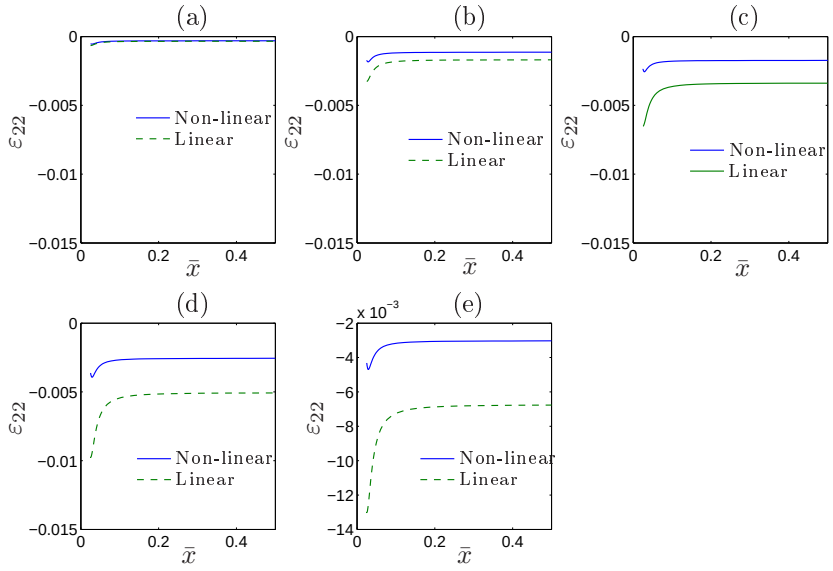

Figure 11: Behaviour of $\varepsilon_{22}(x)$ for the line $y = 0$, $0 \leq x \leq L/2$ using the nonlinear model (Non-linear) and the linearized model (Linear). (a) $\sigma_{\mathrm{V}} = -10^6\,\mathrm{Pa}$, (b) $\sigma_{\mathrm{V}} = -5 \times 10^6\,\mathrm{Pa}$, (c) $\sigma_{\mathrm{V}} = -10^7\,\mathrm{Pa}$, (d) $\sigma_{\mathrm{V}} = -1.5 \times 10^7\,\mathrm{Pa}$, (e) $\sigma_{\mathrm{V}} = -2 \times 10^7\,\mathrm{Pa}$.

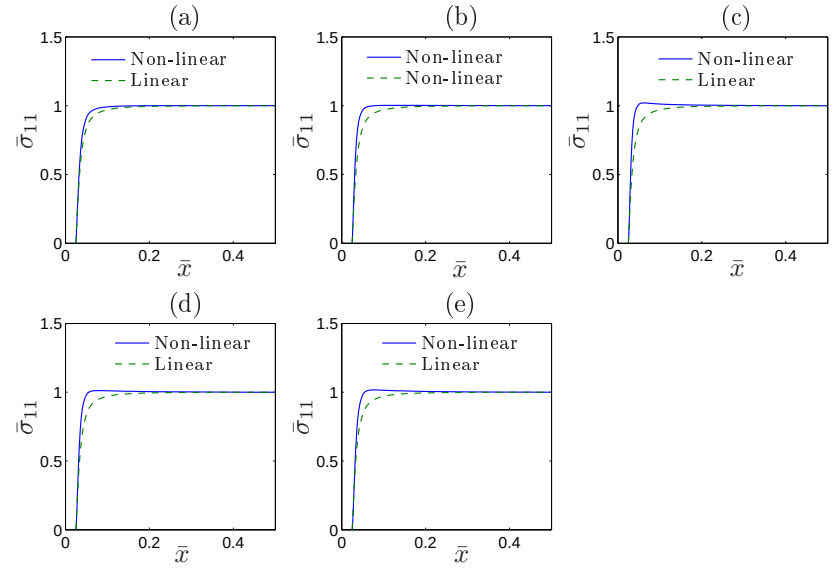

Figure 12: Behaviour of $\bar{\sigma}_{11}$ for the line $y = 0$, $0 \leq x \leq L/2$ using the nonlinear model (Non-linear) and the linearized model (Linear). (a) $\sigma_{\mathrm{V}} = -10^6\,\mathrm{Pa}$, (b) $\sigma_{\mathrm{V}} = -5 \times 10^6\,\mathrm{Pa}$, (c) $\sigma_{\mathrm{V}} = -10^7\,\mathrm{Pa}$, (d) $\sigma_{\mathrm{V}} = -1.5 \times 10^7\,\mathrm{Pa}$, (e) $\sigma_{\mathrm{V}} = -2 \times 10^7\,\mathrm{Pa}$.

Interesting results are observed for $\bar{\sigma}_{22}$. As it is expected, far from the hole σ_{22} also tends to σ_{V}. The maximum for $\bar{\sigma}_{22}$ does not occur at the surface of the hole, as it is predicted by the linearized theory of elasticity, but at a point near that surface. A detailed view of the results presented in

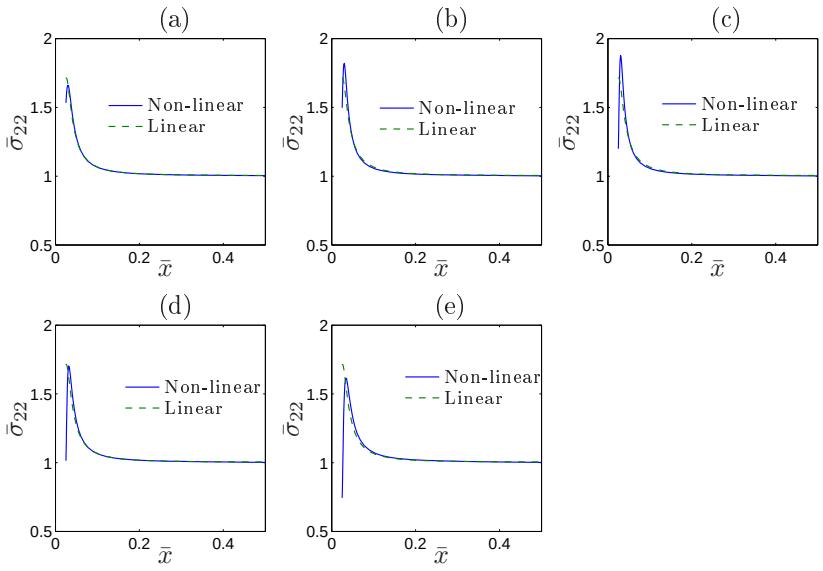

Figure 13: Behaviour of $\bar{\sigma}_{22}$ for the line $y = 0$, $0 \leq x \leq L/2$ using the nonlinear model (Non-linear) and the linearized model (Linear). (a) $\sigma_{\mathrm{V}} = -10^6\,\mathrm{Pa}$, (b) $\sigma_{\mathrm{V}} = -5 \times 10^6\,\mathrm{Pa}$, (c) $\sigma_{\mathrm{V}} = -10^7\,\mathrm{Pa}$, (d) $\sigma_{\mathrm{V}} = -1.5 \times 10^7\,\mathrm{Pa}$, (e) $\sigma_{\mathrm{V}} = -2 \times 10^7\,\mathrm{Pa}$.

Figure 13 is given in Figure 14. The disagreement between the linear and nonlinear models in the prediction of $\bar{\sigma}_{11}$ and $\bar{\sigma}_{22}$ is more noticeable for larger external loads.

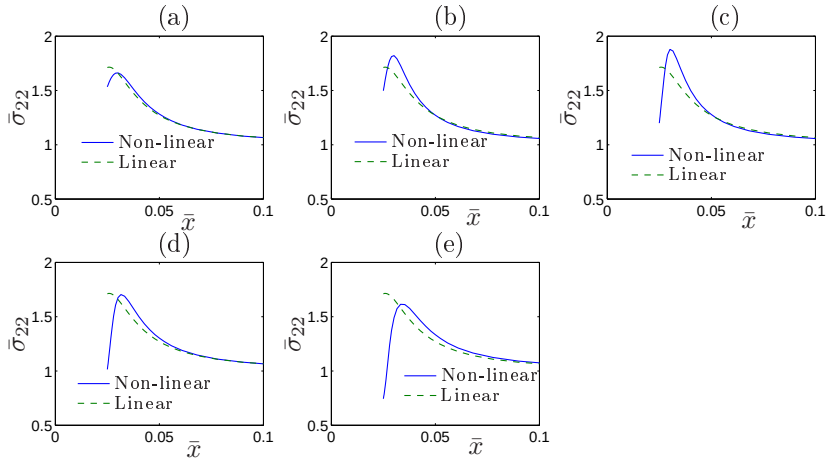

Figure 14: Behaviour of $\bar{\sigma}_{22}$ for the line $y = 0$, $0 \leq x \leq L/2$ using the nonlinear model (Non-linear) and the linearized model (Linear). (a) $\sigma_{\mathrm{V}} = -10^6\,\mathrm{Pa}$, (b) $\sigma_{\mathrm{V}} = -5 \times 10^6\,\mathrm{Pa}$, (c) $\sigma_{\mathrm{V}} = -10^7\,\mathrm{Pa}$, (d) $\sigma_{\mathrm{V}} = -1.5 \times 10^7\,\mathrm{Pa}$, (e) $\sigma_{\mathrm{V}} = -2 \times 10^7\,\mathrm{Pa}$.

In Figures 15-17 results are shown for $\sigma_{\mathrm{H}} = -1.6 \times 10^7\,\mathrm{Pa}$ with $\sigma_{\mathrm{H}} = 2\sigma_{\mathrm{V}}$. Plots for ε_{11}, ε_{22}, $\bar{\sigma}_{11}$ and $\bar{\sigma}_{22}$ as functions of $\bar{y}$ for the line $x = 0$, $0 \leq y \leq L/2$ are presented in Figure 15. There are significant differences between the behaviour of the two components of the stresses as predicted by the two constitutive models. The maxima are not located on the surface of the hole. A detailed

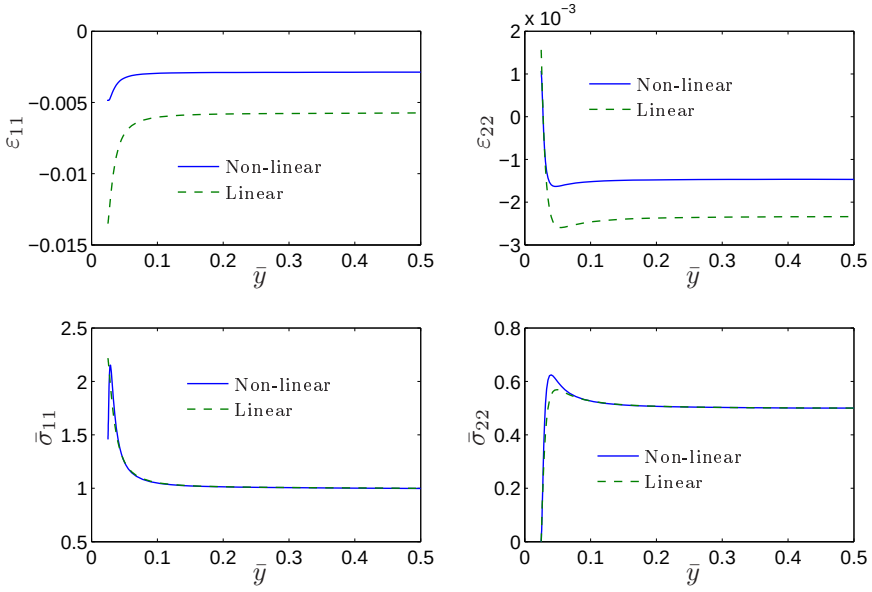

Figure 15: Behaviour of ε_{11}, ε_{22}, $\bar{\sigma}_{11}$ and $\bar{\sigma}_{22}$ for the line $x = 0, 0 \leq y \leq L/2$ for $\sigma_{\mathrm{H}} = -1.6\times10^{7}\,\mathrm{Pa}$ with $\sigma_{\mathrm{H}} = 2\sigma_{\mathrm{V}}$ using the nonlinear model (Non-linear) and the linearized model (Linear).

plot of $\bar{\sigma}_{11}$ and $\bar{\sigma}_{22}$ near the hole is given in Figure 17.

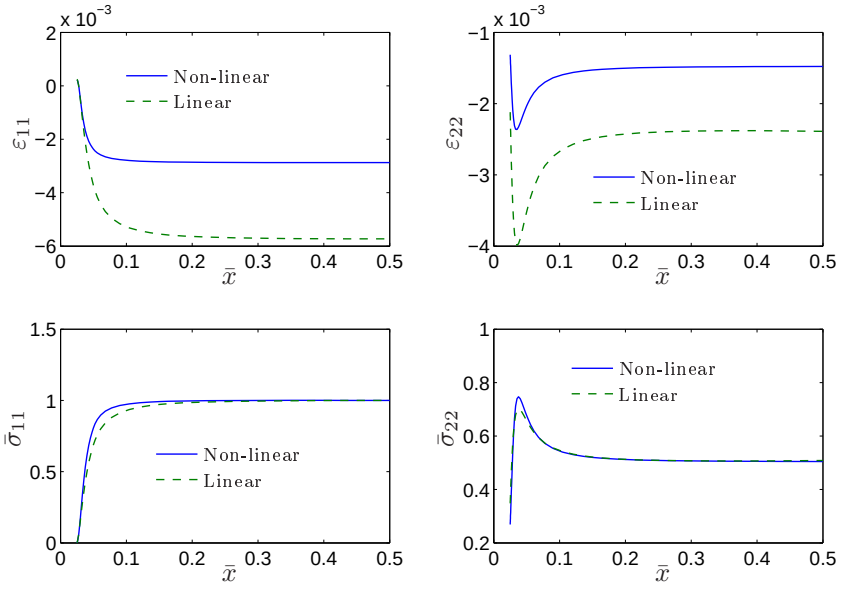

Figure 16: Behaviour of ε_{11}, ε_{22}, $\bar{\sigma}_{11}$ and $\bar{\sigma}_{22}$ for the line $y = 0, 0 \leq x \leq L/2$ for $\sigma_{\mathrm{H}} = -1.6\times10^{7}\,\mathrm{Pa}$ with $\sigma_{\mathrm{H}} = 2\sigma_{\mathrm{V}}$ using the nonlinear model (Non-linear) and the linearized model (Linear).

In Figure 16 results are presented for ε_{11}, ε_{22}, $\bar{\sigma}_{11}$ and $\bar{\sigma}_{22}$ for the line $y = 0$, $0 \leq x \leq L/2$. Details of the behaviour of $\bar{\sigma}_{11}$ and $\bar{\sigma}_{22}$ near the surface of the hole are shown in Figure 17.

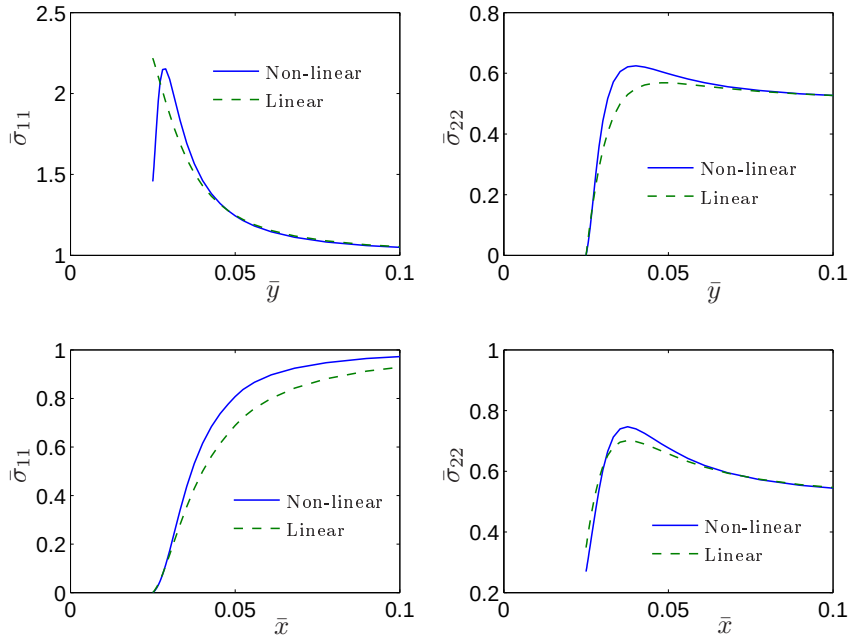

Figure 17: Behaviour of $\bar{\sigma}_{11}$ and $\bar{\sigma}_{22}$ for the lines $y = 0$, $0 \leq x \leq L/2$ and $x = 0$, $0 \leq y \leq L/2$. Details of the behaviour of the different components of the stress near the hole (see Figures 15 and 16).

Finally, in Figure 17 results for $\bar{\sigma}_{11}$ and $\bar{\sigma}_{22}$ are shown for a zone very close to the boundary of the hole.

Comments

The results obtained for this problem that are depicted, for example, in Figures 14 and 17, show that when using the nonlinear constitutive equation (3), the maximum stress (that is usually associated with the failure of rock) does not appear on the surface of the hole, but inside the slab (see Figures 14 and 17 upper left). Additionally, for $\bar{\sigma}_{22}$ depicted in Figure 14, for larger external tractions σ_{V}, the linearized theory of elasticity predicts maximum stresses that are greater than the maximum stresses obtained using the nonlinear model (3). The same happens for $\bar{\sigma}_{11}$ (see the plot on the upper left in Figure 17).

Now, from the experimental point of view, and also from some theoretical and numerical works, there is evidence supporting that damage in rock masses with holes could start inside the rock, and not on the surfaces of the holes[10], as predicted by the linearized theory of elasticity. Also, there is evidence supporting the fact that the linearized constitutive theory overestimates the magnitude of some of the components of the stress, see, for example, Figure 4 in [3], [12], Section 6.6 in [9], Figure 9 in [8] and page 145 in [16].

[10] See, for example, [18], page 190 and Section 3.2 in [3], for a square hole see Figure 13(f) in [33]. See as well Sections 2.2.2, 2.2.3, 4.4.4, pages 176 and 352 in [29] and the references therein.

5 Biaxial compression of a slab with an elliptical hole

In this problem we have a slab similar to the one described in the previous section. It deforms under the influence of uniform vertical and horizontal loads σ_{V}, σ_{H}. There is an elliptic hole with principal axes a, b. It is assumed that $b \gg a$, i.e., the elliptical hole is an approximation of a crack, and it is assumed that the principal axis b is horizontal and aligned with the coordinate x (see Figure 5). We assume plane strains, $\sigma_{\mathrm{H}} = 2\sigma_{\mathrm{V}}$ and $L = 100\,\mathrm{m}$, $b = 10\,\mathrm{m}$ and $\frac{b}{a} = 40$.

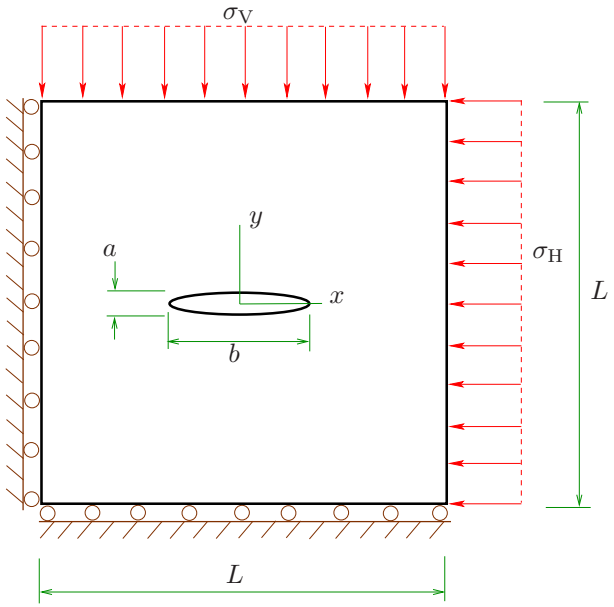

Figure 18: Square slab with a central elliptical hole under biaxial compression. Plane strain condition is assumed. The main axis of the hole is aligned with the coordinate system.

In Figures 10SM-14SM results are presented for the components σ_{11}, σ_{22} and σ_{12} of the stress tensor, and the principal stresses σ_1 and σ_2 when[11] $\sigma_{\mathrm{H}} = -6 \times 10^5\,\mathrm{Pa}$ using the linear constitutive model (5) and the nonlinear constitutive equation (3). The results are presented only for a small region around the point $x = b/2$, $y = 0$, which is the tip of the elliptic hole. From the results we observe that the magnitudes of the stresses predicted by the nonlinear constitutive model (3) are higher than those predicted by the linearized model (5).

In Figures 13SM and 14SM results are presented for the principal stresses σ_1 and σ_2 when $\sigma_{\mathrm{H}} = -6 \times 10^5\,\mathrm{Pa}$. The results shown in Figure 13SM are particularly interesting. It is observed that for the nonlinear model, the magnitude of σ_1 when $\sigma_1 > 0$ (which appears near the boundary of the hole) is greater than the one obtained using the linearized model. Finally, in Figure 14SM in the Supplementary Material results are presented for σ_2 as predicted by the nonlinear model (3) and the linearized equation (5). In both cases the stress is negative, but its magnitude is higher when using the nonlinear model.

In Figures 19-22 results are shown for ε_{11}, ε_{22}, and the dimensionless stresses $\bar{\sigma}_{11}$, $\bar{\sigma}_{22}$, for different external traction σ_{H}. The plots are presented for the line $y = 0$, $b/2 \leq x$ very close to the boundary of the hole. In Figures 19 and 20 it is noticed slight differences for the behaviour of ε_{11}. For ε_{22} it is observed that the magnitude of the strains are smaller when using the nonlinear model. For $\bar{\sigma}_{11}$, Figure 21 reveals a greater difference between the predictions of the linear and nonlinear models for higher values of σ_{H}. The same occurs for $\bar{\sigma}_{22}$ (see Figure 22). The maximum for $\bar{\sigma}_{22}$ is observed in 22 36(c) and it appears inside the slab.

[11] This external traction was the maximum load that it was possible to apply without having problems with the convergence of the numerical solution.

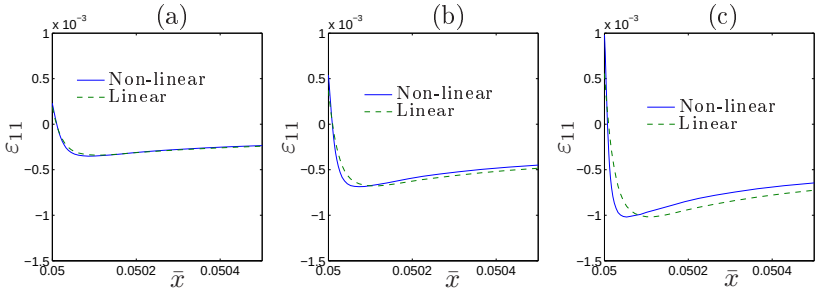

Figure 19: Behaviour of ε_{11} for the line $y = 0$ using nonlinear model (Non-linear) and the linearized model (Linear). (a) $\sigma_{\mathrm{H}} = -2 \times 10^5\,\mathrm{Pa}$, (b) $\sigma_{\mathrm{H}} = -4 \times 10^5\,\mathrm{Pa}$, (c) $\sigma_{\mathrm{H}} = -6 \times 10^5\,\mathrm{Pa}$.

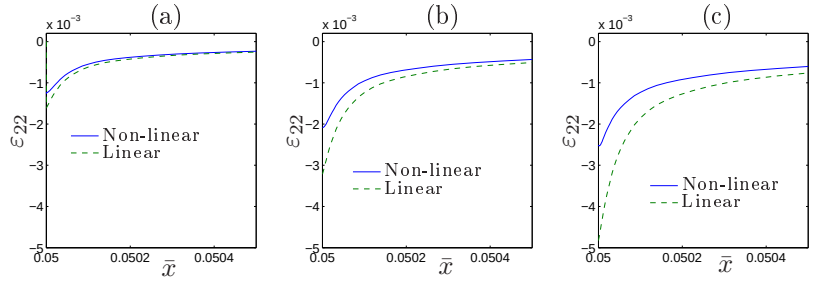

Figure 20: Behaviour of ε_{22} for the line $y = 0$ using the nonlinear model (Non-linear) and the linearized model (Linear). (a) $\sigma_{\mathrm{H}} = -2 \times 10^5\,\mathrm{Pa}$, (b) $\sigma_{\mathrm{H}} = -4 \times 10^5\,\mathrm{Pa}$, (c) $\sigma_{\mathrm{H}} = -6 \times 10^5\,\mathrm{Pa}$.

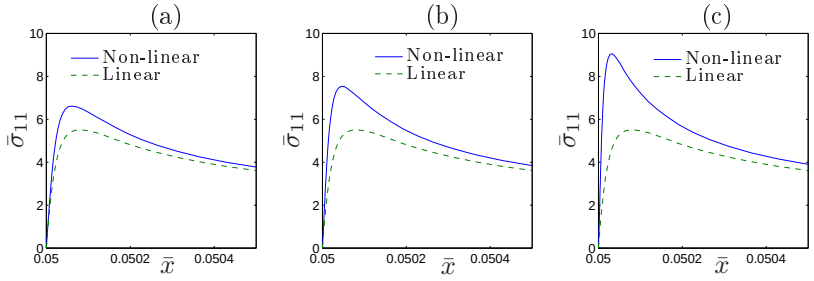

Figure 21: Behaviour of $\bar{\sigma}_{11}$ for the line $y = 0$ using the nonlinear model (Non-linear) and the linearized model (Linear). (a) $\sigma_{\mathrm{H}} = -2 \times 10^5\,\mathrm{Pa}$, (b) $\sigma_{\mathrm{H}} = -4 \times 10^5\,\mathrm{Pa}$, (c) $\sigma_{\mathrm{H}} = -6 \times 10^5\,\mathrm{Pa}$.

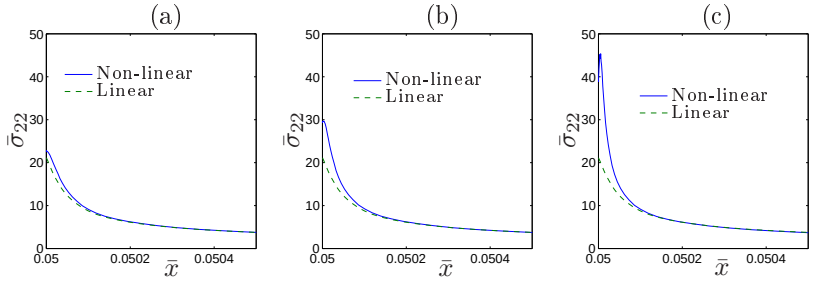

Figure 22: Behaviour of $\bar{\sigma}_{22}$ for the line $y = 0$ using the nonlinear model (Non-linear) and the linearized model (Linear). (a) $\sigma_{\mathrm{H}} = -2 \times 10^5\,\mathrm{Pa}$, (b) $\sigma_{\mathrm{H}} = -4 \times 10^5\,\mathrm{Pa}$, (c) $\sigma_{\mathrm{H}} = -6 \times 10^5\,\mathrm{Pa}$.

Additional results were obtained for the same components of the strain and dimensionless stresses for the line $x = 0$, $a/2 \leq y \leq L/2$. From those results, it was possible to see almost an agreement between the predictions of the two constitutive models. This is not surprising as the stress concentration is low $x = 0$, $y = a/2$ and therefore it is not expected to be otherwise. For the sake of brevity such results are not shown here.

Comments

The geometries studied in this and in the next section are approximations of cracks in rock masses under biaxial compression. The main goal is to compare the predictions of the nonlinear constitutive equation (3) and the linear model (5), especially regarding the maximum stresses and where they appear. From Figures 10SM-12SM we can see that the maximum magnitude for the stresses are larger (in magnitude) when using the nonlinear constitutive equation.

Particularly interesting are the results depicted in Figure 13SM, where the magnitude of the first principal stress can be very large in comparison with the results using the linearized model, for the region where $\sigma_1 > 0$. It is necessary to recall that rock is a material that cannot support large positive stresses (tension) in contrast with compression (see, for example, Section 1.2.3 in [2]). That the nonlinear constitutive equation (3) predicts such higher positive values for that principal stress is a factor, which should be studied in a deeper manner from the experimental point of view.

From Figure 21 and 22 it is observed in a more precise manner that the nonlinear model predicts larger (in magnitude) values for the normal stress. Interestingly, in Figure 22(c) such maximum happens not on the surface of the elliptical hole, but slightly inside it. This implies that if $\bar{\sigma}_{22}$ would be used to predict the rupture of the rock mass, that rupture would happen inside the body, which is something similar to what is observed for the problem studied in Section 4.

For the case of the slab with an inclined elliptical hole (see Figure 15SM) results are obtained for σ_{11}, σ_{22}, σ_{12}, σ_1 and σ_2 for $\sigma_{\mathrm{H}} = -10^5\,\mathrm{Pa}$. The predictions with the two models are almost in agreement, and thus these results are not presented here[12]. In Figures 16SM and 17SM results are shown for σ_{12} and the principal stress σ_1, for a small area near the tip of the elliptic hole. Some differences are found between the predictions of the linear and nonlinear models. For σ_{12} its predicted magnitude is higher when the nonlinear model is used. The results for σ_1, which are depicted in Figure 17SM, are more interesting. In contrast to the predictions of the nonlinear model, the linear model predicts that σ_1 is always negative. In Figure 17SM (on the right), there is a narrow region near the boundary of the hole where σ_1 is positive. The presence of such positive stresses could have an important impact on the modelling of failure near the tips of cracks since, in general, rock cannot support higher tensile stresses (see the comments at the end of the previous section). Considering the geometry of the problem depicted in Figure 15SM, in this section no additional plots are presented.

6 Slab with an elliptical hole subjected to shear

In this section, the behaviour of a slab with an elliptic hole subjected to a uniform shear stress τ_o on its upper surface (see Fig. 23) is studied. The lower surface of the slab cannot displace. The geometry of the slab and the elliptic hole is the same as defined in Section 5. The hole can be seen as an approximation of a crack under the effect of a distant uniform shear stress. The body shown in Figure 23 is also very long in the direction z so that plane strain condition is assumed. The following dimensionless stresses are defined:

$$\bar{\sigma}_{11} = \frac{\sigma_{11}}{\tau_o}, \quad \bar{\sigma}_{22} = \frac{\sigma_{22}}{\tau_o}. \tag{14}$$

[12] In those three cases, it was observed that the magnitude of the predicted stresses when using the nonlinear model was slightly higher than the predictions of the linear model.

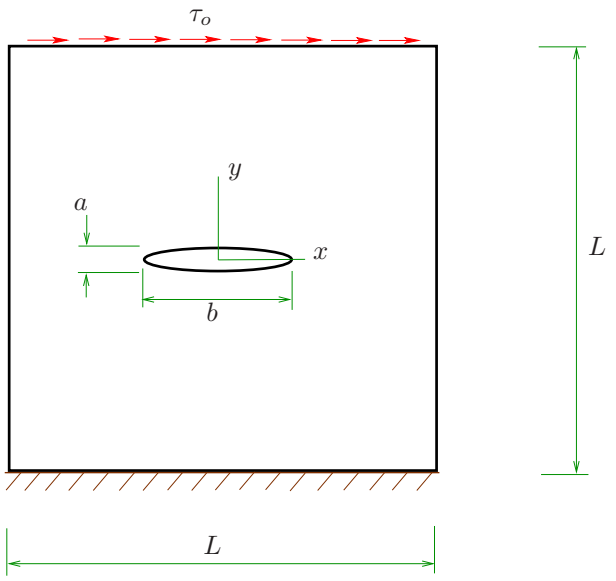

Figure 23: Slab with a central elliptical hole under shear.

In Figures 18SM-22SM results are presented for σ_{11}, σ_{22}, σ_{12} and the principal stresses σ_1, σ_2 when[13] $\tau_o = 1.8 \times 10^5$ Pa, where the predictions using the linear and the nonlinear constitutive models, (5) and (3), respectively, are compared. For σ_{11} and σ_{22} their maximum magnitude can be significantly large in the zone they are negative. The predictions of the nonlinear model indicate that the absolute magnitude of the stresses is higher than the corresponding values that are obtained when the linear constitutive model is used. For σ_{12} the difference in behaviour is more notorious. For example, from the predictions of the nonlinear model in Figure 20SM, the maximum positive stress is more than four times greater than the value that is obtained when the linear model is used. For the negative values of the stress, the predicted value when using the nonlinear model is $\sigma_{12_{max}} = -1.0132 \times 10^5$ Pa, whereas $\sigma_{12_{max}} = -246$ Pa when using the linear model.

Figures 21SM and 22SM present the results for the two principal stresses. For σ_1 a notorious difference between the predictions of the two models is observed when σ_1 is negative. Figure 21SM shows that the results for σ_1 that are obtained using the nonlinear model are approximately four times greater (in magnitude) than the predictions of the linear model. Something similar happens with σ_2 as observed in Figure 22SM.

In Figures 24-29 results are shown for ε_{11}, ε_{22}, ε_{12}, $\bar{\sigma}_{11}$, $\bar{\sigma}_{22}$ and $\bar{\sigma}_{12}$, for the line $y = 0$, $b/2 \leq x$ near the tip of the elliptic hole. Different values for the external load τ_o are used. The results for the strain tensor are depicted in Figures 24-26. An important difference in the behaviour is observed when comparing the predictions of the nonlinear and the linearized models. In particular, for ε_{12} the nonlinear model predicts lower magnitudes than the linearized model, as shown in Figure 26.

In Figure 27, results for $\bar{\sigma}_{11}$ are presented. The absolute magnitude of $\bar{\sigma}_{11}$ that is predicted by the nonlinear model is greater than the prediction of the linearized model. Regarding $\bar{\sigma}_{22}$ Figure 28 shows that the maximum values (in magnitude) are all located on the boundary of the hole (at $x = b/2$, $y = 0$). Similar to the results for $\bar{\sigma}_{11}$, the magnitude of $\bar{\sigma}_{22}$ is greater when the nonlinear model is used. Finally, for $\bar{\sigma}_{12}$, as in the previous cases, the magnitude of the stresses is greater when using the nonlinear model (see Figure 29).

In Figures 30 and 31 results are shown for ε_{12} and $\bar{\sigma}_{12}$ for the line $x = 0$, $a/2 \leq y \leq L/2$

[13] As in the problems presented in the previous sections, this specific value for τ_o was the maximum stress such that there is convergence for the numerics.

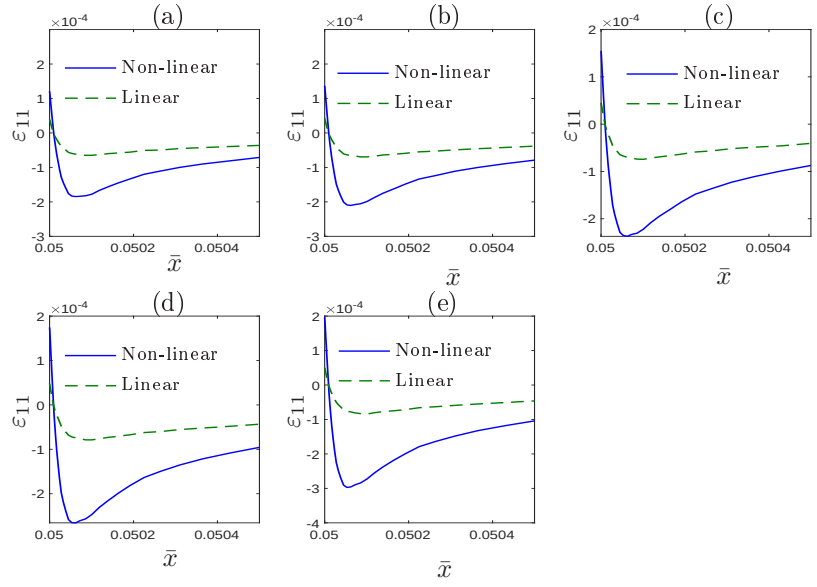

Figure 24: Behaviour of ε_{11} for the line $y = 0$ using the nonlinear model (Non-linear) and the linearized model (Linear). (a) $\tau_o = 1.4 \times 10^5$ Pa, (b) $\tau_o = 1.5 \times 10^5$ Pa, (c) $\tau_o = 1.6 \times 10^5$ Pa, (c) $\tau_o = 1.7 \times 10^5$ Pa, (c) $\tau_o = 1.8 \times 10^5$ Pa.

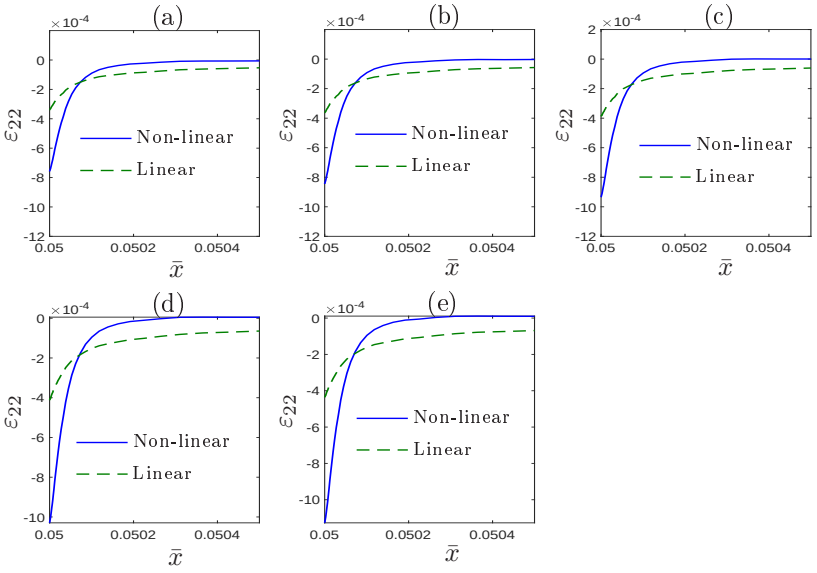

Figure 25: Behaviour of ε_{22} for the line $y = 0$ using the nonlinear model (Non-linear) and the linearized model (Linear). (a) $\tau_o = 1.4 \times 10^5$ Pa, (b) $\tau_o = 1.5 \times 10^5$ Pa, (c) $\tau_o = 1.6 \times 10^5$ Pa, (c) $\tau_o = 1.7 \times 10^5$ Pa, (c) $\tau_o = 1.8 \times 10^5$ Pa.

and external loads τ_o. In both cases a noticeable difference appears when comparing the results predicted by the nonlinear and the linearized constitutive models.

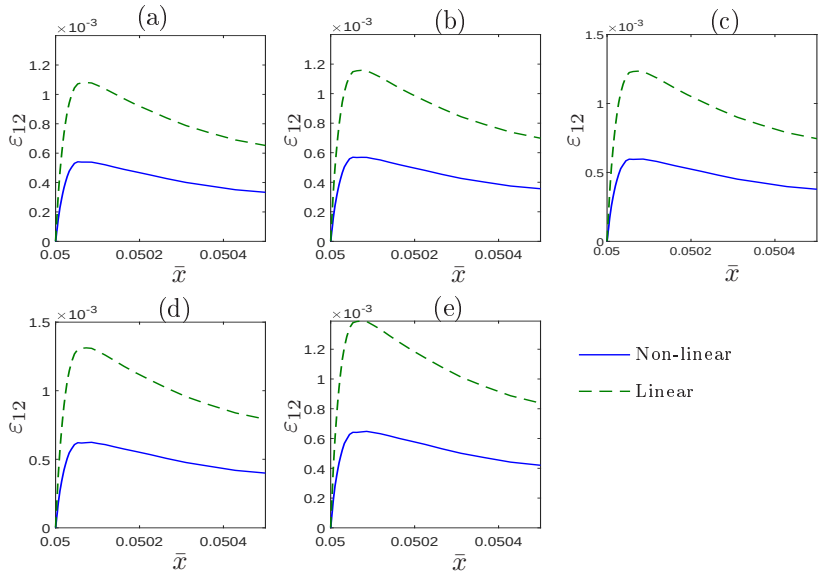

Figure 26: Behaviour of ε_{12} for the line $y = 0$ using the nonlinear model (Non-linear) and the linearized model (Linear). (a) $\tau_o = 1.4 \times 10^5$ Pa, (b) $\tau_o = 1.5 \times 10^5$ Pa, (c) $\tau_o = 1.6 \times 10^5$ Pa, (c) $\tau_o = 1.7 \times 10^5$ Pa, (c) $\tau_o = 1.8 \times 10^5$ Pa.

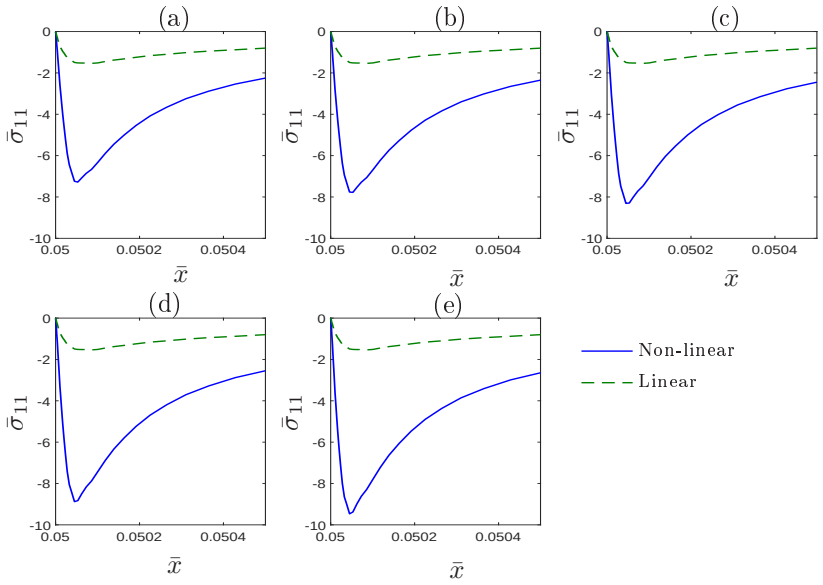

Figure 27: Behaviour of $\bar{\sigma}_{11}$ for the line $y = 0$ using the nonlinear model (Non-linear) and the linearized model (Linear). (a) $\tau_o = 1.4 \times 10^5$ Pa, (b) $\tau_o = 1.5 \times 10^5$ Pa, (c) $\tau_o = 1.6 \times 10^5$ Pa, (d) $\tau_o = 1.7 \times 10^5$ Pa, (e) $\tau_o = 1.8 \times 10^5$ Pa.

Comments

The magnitude of the components of the stresses σ_{11}, σ_{22} and σ_{12} are greater when using the nonlinear model. Unlike the results obtained in the problems studied in the previous section,

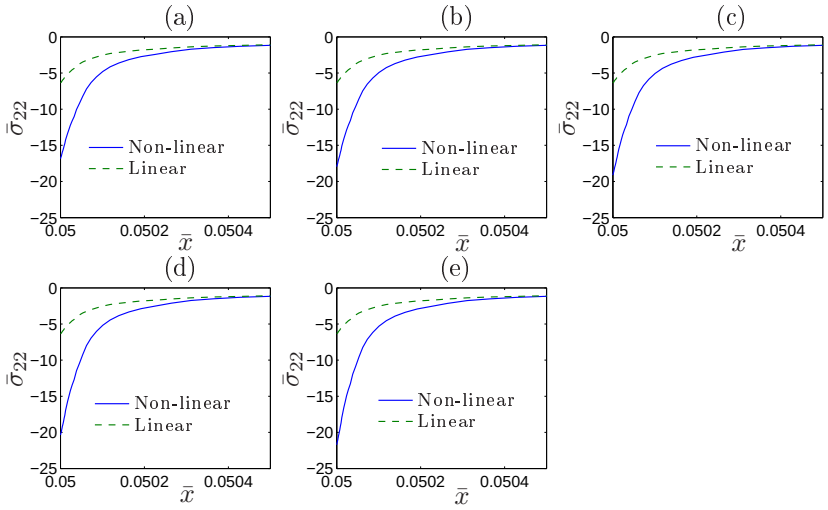

Figure 28: Behaviour of $\bar{\sigma}_{22}$ for the line $y = 0$ using the nonlinear model (Non-linear) and the linearized model (Linear). (a) $\tau_o = 1.4 \times 10^5\,\text{Pa}$, (b) $\tau_o = 1.5 \times 10^5\,\text{Pa}$, (c) $\tau_o = 1.6 \times 10^5\,\text{Pa}$, (d) $\tau_o = 1.7 \times 10^5\,\text{Pa}$, (e) $\tau_o = 1.8 \times 10^5\,\text{Pa}$.

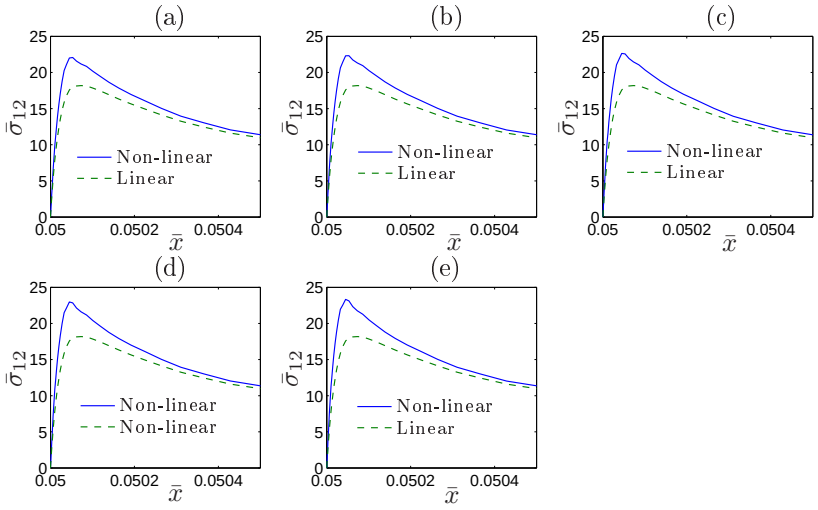

Figure 29: Behaviour of $\bar{\sigma}_{12}$ for the line $y = 0$ using the nonlinear model (Non-linear) and the linearized model (Linear). (a) $\tau_o = 1.4 \times 10^5\,\text{Pa}$, (b) $\tau_o = 1.5 \times 10^5\,\text{Pa}$, (c) $\tau_o = 1.6 \times 10^5\,\text{Pa}$, (d) $\tau_o = 1.7 \times 10^5\,\text{Pa}$, (e) $\tau_o = 1.8 \times 10^5\,\text{Pa}$.

here the maximum value for σ_{22} does not appear inside the slab, but on the boundary of the elliptical hole. It is not known whether a maximum value for that component of the stress would be obtained inside the slab if a larger τ_o were applied. On the other hand, it is interesting to notice that for the upper surface of the elliptical hole, for the line $x = 0$, the shear stress σ_{12} is smaller when using the nonlinear model.

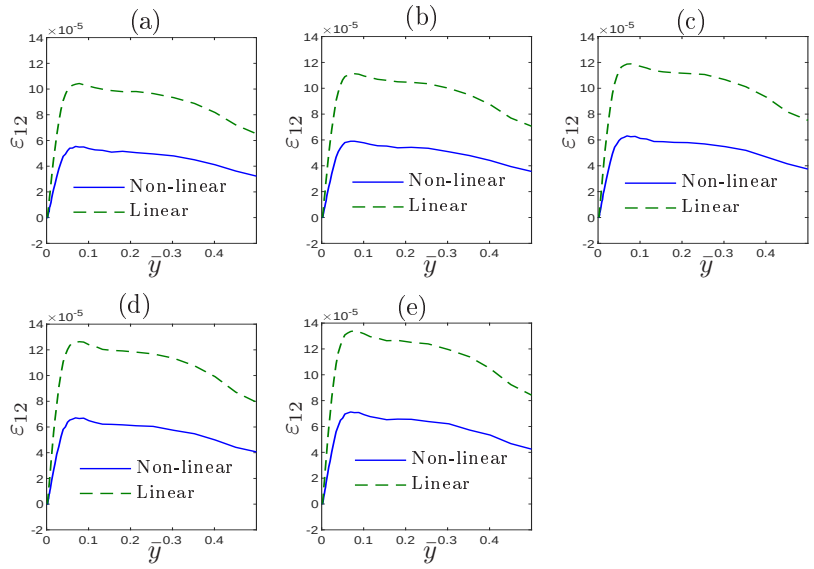

Figure 30: Behaviour of ε_{12} for the line $x = 0$ using the nonlinear model (Non-linear) and the linearized model (Linear). (a) $\tau_o = 1.4 \times 10^5$ Pa, (b) $\tau_o = 1.5 \times 10^5$ Pa, (c) $\tau_o = 1.6 \times 10^5$ Pa, (d) $\tau_o = 1.7 \times 10^5$ Pa, (e) $\tau_o = 1.8 \times 10^5$ Pa.

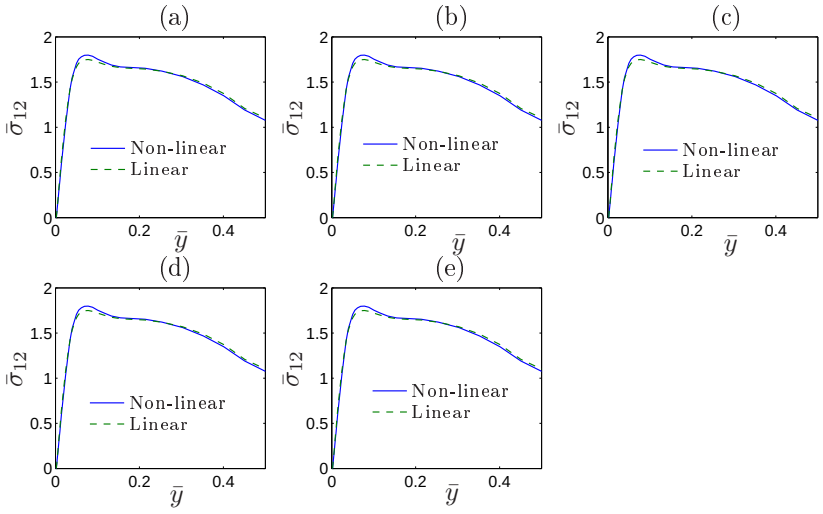

Figure 31: Behaviour of $\bar{\sigma}_{12}$ for the line $x = 0$ using the nonlinear model (Non-linear) and the linearized model (Linear). (a) $\tau_o = 1.4 \times 10^5$ Pa, (b) $\tau_o = 1.5 \times 10^5$ Pa, (c) $\tau_o = 1.6 \times 10^5$ Pa, (d) $\tau_o = 1.7 \times 10^5$ Pa, (e) $\tau_o = 1.8 \times 10^5$ Pa.

7 Final remarks

Rock is a material that can show a complex mechanical behaviour, such as dissimilar behaviour when comparing uniaxial compression and uniaxial tension. It can also exhibit a nonlinear behaviour, presenting a stiffness that increases with the application of an external compressive load. It is argued that the aforementioned phenomena is related to the closure of cracks and pores

inside, which are present in most types of rock. The same cracks and pores can make rock less stiff in tension, which is the reason most types of rock present a lower Young's modulus in tension than in compression [12]. The relatively new constitutive theories developed by Rajagopal and co-workers [22, 23, 27, 25, 24, 28, 6] have great potentials to be used in this class of material. The purpose of this article was to assess the predictions of the new constitutive equation proposed in [6] and benchmark these predictions with those of the linearized model. Some of the results obtained agree qualitatively with some experimental evidence, but more work is necessary to ascertain the appropriateness of this new kind of constitutive equation for these problems. Also, the interpretation of many experiments, such as the bending of a beam, or the Brazilian test, depends on the constitutive model used [8]. These experiments should be studied in the light of this new constitutive model. We plan to cover them as part of future work.

Acknowledgment

This research was conducted under the auspices of FONDECYT (Chile) through grant no. 1160030.

References

[1] Adler, L. (1970). Evaluating double elasticity in drill cores under flexure. International Journal of Rock Mechanics and Mining Sciences and Geomechanics Abstracts, 7, 357–370.

[2] Brady, B.H.G., & Brown, E.T. (2005). Rock Mechanics for Underground Mining. Kluwer Academic Publishers, New York, Boston, Dorchecht, London, Moscow.

[3] Bron, E.T, Bray, J.W., & Santarelli, F.J. (1989). Influence of stress-dependent elastic moduli on stresses and strains around axilsymmetric boreholes. Rock Mechanics and Rock Engineering, 22, 189–203.

[4] Bustamante, R., & Rajagopal, K.R. (2010). A note on plane strain and plane stress problems for a new class of elastic bodies. Mathematics and Mechanics of Solids, 15, 229–238.

[5] Bustamante, R., & Rajagopal, K.R. (2015). A note on some new classes of constitutive relations for elastic bodies. IMA Journal of Applied Mathematics, 80, 1287–1299.

[6] Bustamante, R., & Rajagopal, K.R. (2018). A nonlinear model describing the mechanical behaviour of rock. Acta Mechanica, 229, 251–272.

[7] Bustamante, R., & Rajagopal, K.R. (2020) A Review of Implicit Constitutive Theories to Describe the Response of Elastic Bodies. In Constitutive Modelling of Solid Continua, Eds. J. Merodio and R.W. Ogden. Springer International Publishing, 187–230.

[8] Cates, B.J. (1992). Size and sress gradient effects on fracture around cavities. Rock Mechanics and Rock Engineering, 25, 167–186.

[9] Chen, R. (1993). In situ and laboratory studies of potash deformation. PhD Thesis, Department of Civil Engineering, The University of Manitoba.

[10] Devendiran, V.K., Sandeep, R.K., Kannan, K., & Rajagopal, K.R. (2017). A thermodinamically consistent constitutive equation for describing the response exhibited by several alloys and the study of a meaningful physical problem. International Journal of Solids and Structures, 108, 1–10.

[11] Grasley, Z., El-Helou, R., D'Amborsia, M., Mokarem, D., Moen, C., & Rajagopal, K.R. (2015). Model of infinitesimal nonlinear elastic response of concrete subjected to uniaxial compression. Journal of Engineering Mechanics, 141, 04015008.

[12] Haimson, B.C., & Tharp, T.M. (1974). Stresses around boreholes in bilinear elastic rocks. Society of Petroleum Engineers Journal, V14, 145–151.

[13] Hawkes, I., & Mellor, M. (1970). Uniaxial testing in rock mechanics laboratories. Engineering Geology, 4, 177–285.

[14] Guyer, R.A., & Johnson, P.A. (2009). Nonlinear mesoscopic elasticity: The complex behaviour of granular media including rocks and soil. Wiley-VCH Verlag GmbH & Co. KGaA Weinheim.

[15] Johnson, P.A., & Rasolofosaon, P.N.J. (1996). Manifestation of nonlinear elasticity in rock: Convincing evidence over large frequency and strain intervals from laboratory studies. Nonlinear Processes in Geophysics, 3, 77–88.

[16] Kaiser, P.K., Guenot, A., & Morgensten, N.R. (1985). Deformation of small tunnels-IV. Behaviour during failure. International Journal of Rock Mechanics and Mining Sciences and Geomechanics Abstracts, 22, 141–152.

[17] Kulvait, V., Málek, J., & Rajagopal, K.R. (2017). Modelling gum metal and other newly developed titanium alloys within a new class of constitutive relations for elastic bodies. Archives of Mechanics, 69, 223–241.

[18] Maury, V. (1987). Observations, rechercher et resultats recent sur les mecanisms de rupture autour de galeries isolees. Rapport de la Commission SMIR sur les mecanismes de rupture autour d'ovrages souterrains. Proceedings of the 6th Congress of the International Society of Rock Mechanics Montreal, Rotterdam, Nalkema 1119–1128.

[19] Okubo, S., & Nishimatsu, Y. (1985). Uniaxial compression testing using a linear combination of stress and strain as the control variable. International Journal of Rock Mechanics and Mining Sciences and Geomechanics Abstracts, 22, 323–330.

[20] Okubo, S., & Fukui, K. (1996). Complete stress-strain curves for various rock types in uniaxial tension. International Journal of Rock Mechanics and Mining Sciences and Geomechanics Abstracts, 33, 549–556.

[21] Ortiz, A., Bustamante, R., & Rajagopal, K.R. (2012). A numerical study of a plate with a hole for a new class of elastic bodies. Acta Mechanica, 223, 1971–1981.

[22] Rajagopal, K.R. (2003). On implicit constitutive theories. Applications of Mathematics, 48, 279–319.

[23] Rajagopal, K.R. (2007). The elasticity of elasticity. Zeitschrift für Angewandte Mathematik und Physik, 58, 309–317.

[24] Rajagopal, K.R. (2011). Non-linear elastic bodies exhibiting limiting small strain. Mathematics and Mechanics of Solids, 16, 122–139.

[25] Rajagopal, K.R. (2011). Conspectus of concepts of elasticity. Mathematics and Mechanics of Solids, 16, 536–562.

[26] Rajagopal, K.R. (2014) On the nonlinear elastic response of bodies on the small strain range. Acta Mech. 225, 1545–1553.

[27] Rajagopal, K.R., & Srinivasa, A.R. (2007). On the response of non-dissipative solids. Proceedings of the Royal Society of London. Series A, 463, 357–367.

[28] Rajagopal, K.R., & Srinivasa, A.R. (2009). On a class of non-dissipative materials that are not hyperelastic. Proceedings of the Royal Society of London. Series A, 465, 493–500.

[29] Santarelli, F.J. (1987). Theoretical and experimental investigation of the stability of the axisymmetric wellbore. PhD Thesis, Faculty of Engineering, Imperial College of London.

[30] Truesdell, C.A., & Toupin, R. (1960) The Classical Theories. In: Flügge S. (ed). Handbuch der Physik, vol. III/I. Springer, Berlin, pp. 226–902.

[31] Truesdell, C.A., & Noll, W. (2004). The Non-linear Field Theories of Mechanics. Third Edition, Antmann S.S. (ed). Springer-Verlag, Berlin Heidelberg .

[32] Yang, S.Q. (2016). Experimental study on deformatin, peak strength and crack damage behavior of hollow sandstone under conventional triaxial compression. Engineering Geology, 213, 11–24.

[33] Zeng, W., Yang, S.Q., & Tian, W.L. (2018). Experimental and numerical investigation of brittle sandstone specimen containing different shapes of holes under uniaxial compression. Engineering Fracture Mechanics, 200, 430–450.